Royal Astronomic Society

MNRAS **532**, 3222–3235 (2024) Advance Access publication 2024 July 11

# Comparison of models for the warm-hot circumgalactic medium around Milky Way-like galaxies

Priyanka Singh <sup>6</sup>, <sup>1,2,3</sup>★ Erwin T. Lau <sup>6</sup>, <sup>4,5</sup>★ Yakov Faerman, <sup>6</sup> Jonathan Stern <sup>6</sup> and Daisuke Nagai <sup>6</sup>, <sup>1,2</sup>

Accepted 2024 July 8. Received 2024 July 6; in original form 2024 May 23

#### **ABSTRACT**

A systematic comparison of the models of the circumgalactic medium (CGM) and their observables is crucial to understanding the predictive power of the models and constraining physical processes that affect the thermodynamics of CGM. This paper compares four analytic CGM models: precipitation, isentropic, cooling flow, and baryon pasting models for the hot, volume-filling CGM phase, all assuming hydrostatic or quasi-hydrostatic equilibrium. We show that for fiducial parameters of the CGM of a Milky Way (MW)-like galaxy ( $M_{\rm vir} \sim 10^{12}~{\rm M}_{\odot}$  at  $z \sim 0$ ), the thermodynamic profiles – entropy, density, temperature, and pressure – show most significant differences between different models at small ( $r \lesssim 30~{\rm kpc}$ ) and large scales ( $r \gtrsim 100~{\rm kpc}$ ) while converging at intermediate scales. The slope of the entropy profile, which is one of the most important differentiators between models, is  $\approx 0.8$  for the precipitation and cooling flow models, while it is  $\approx 0.6$  and 0 for the baryon pasting and isentropic models, respectively. We make predictions for various observational quantities for an MW mass halo for the different models, including the projected Sunyaev–Zeldovich effect, soft X-ray emission (0.5–2 keV), dispersion measure, and column densities of oxygen ions (O VI, O VII, and O VIII) observable in absorption. We provide Python packages to compute the thermodynamic and observable quantities for the different CGM models.

**Key words:** galaxies: clusters: intracluster medium – galaxies: haloes.

### 1 INTRODUCTION

A large fraction of baryons associated with galactic haloes reside in a gaseous phase, extending out and potentially beyond the virial radius of the halo. This gaseous halo is referred to as the intracluster medium (ICM) in clusters of galaxies, the intra-group medium (IGrM) in galaxy groups, and the circumgalactic medium (CGM) around galaxies (see Tumlinson, Peeples & Werk 2017 for review). Amongst these, the CGM is the most poorly constrained regime observationally owing to its lower density and temperature than the IGrM and ICM and theoretically due to the major impact of nongravitational processes such as feedback and turbulence.

The CGM can be studied across multiple wavelengths, ranging from microwave (Prochaska & Zheng 2019), ultraviolet (UV; Werk et al. 2013; Lehner, Howk & Wakker 2015; Qu & Bregman 2018; Chen et al. 2020; Tchernyshyov et al. 2022), to X-rays (Anderson, Churazov & Bregman 2016; Li et al. 2018; Das et al. 2021). More recently, Bregman et al. (2022) detected resolved thermal Sunyaev–Zeldovich (tSZ) profiles from  $L^*$  galaxies, constraining their hot

\* E-mails: psingh@iiti.ac.in (PS); erwin.lau@cfa.harvard.edu (ETL)

baryon budget. Chadayammuri et al. (2022) and Comparat et al. (2022) stacked star-forming and passive galaxies in the extended ROentgen Survey with an Imaging Telescope Array (eROSITA) Final Equatorial Depth Survey (eFEDS), and Zhang et al. (2024) stacked central and isolated galaxies in the first data release of the eROSITA all sky survey (eRASS), measuring the resolved X-ray surface brightness profiles from the CGM. These observations have pushed the detection capabilities to new limits (i.e. resolving the radial distribution of the CGM down to Milky Way (MW) masses).

Both the quality and quantity of CGM measurements are expected to take another leap with ongoing and upcoming experiments, such as the Canadian Hydrogen Intensity Mapping Experiment (CHIME, CHIME/FRB Collaboration 2018) and the Hydrogen Intensity and Real-time Analysis eXperiment (Newburgh et al. 2016) in the radio, detecting the dispersion measure from Fast Radio Bursts (FRBs), the Advanced Atacama Cosmology Telescope (AdvACT; Henderson et al. 2016), South Pole Telescope-3G (SPT-3G; Benson et al. 2014), Simons Observatory (Ade et al. 2019), and cosmic microwave background (CMB)-S4 (Abazajian et al. 2016) at mm wavelength detecting the SZ effect, and eRASS in the X-ray. Through SZ and X-ray surveys, we will probe the resolved CGM profiles to the

<sup>&</sup>lt;sup>1</sup>Yale Center for Astronomy & Astrophysics, New Haven, CT 06511, USA

<sup>&</sup>lt;sup>2</sup>Department of Physics, Yale University, New Haven, CT 06520, USA

<sup>&</sup>lt;sup>3</sup>Department of Astronomy, Astrophysics and Space Engineering, Indian Institute of Technology, Indore 453552, India

<sup>&</sup>lt;sup>4</sup>Center for Astrophysics|Harvard & Smithsonian, 60 Garden St, Cambridge, MA 02138, USA

<sup>&</sup>lt;sup>5</sup>Department of Physics, University of Miami, Coral Gables, FL 33124, USA

<sup>&</sup>lt;sup>6</sup>Astronomy Department, University of Washington, Seattle, WA 98195, USA

<sup>&</sup>lt;sup>7</sup>School of Physics & Astronomy, Tel Aviv University, Tel Aviv 69978, Israel

virial radii of  $M_{\rm vir}\sim 10^{12}~{\rm M}_{\odot}$  galaxies. At the same time, ongoing and upcoming FRB observations will push the mass limit down to  $M_{\rm vir}\sim 10^{11}~{\rm M}_{\odot}$  (Battaglia et al. 2019; Wu & McQuinn 2022). Therefore, on the theoretical modelling front, we need to prepare ourselves to maximize the CGM physics extracted through these next-generation missions.

Several theoretically and observationally motivated models have been developed to describe and study the dominant physical processes that govern the CGM (e.g. Voit et al. 2017; Choudhury, Sharma & Quataert 2019; Stern et al. 2019; Faerman, Sternberg & McKee 2020; Singh, Voit & Nath 2021; Pandya et al. 2023). These models represent a simplified approach to modelling CGM thermodynamics. Hydrodynamical cosmological simulations, on the other hand, capture a more realistic and complex interplay between the different processes in the CGM (e.g. Oppenheimer 2018; Hafen et al. 2019; Hummels et al. 2019; Peeples et al. 2019; van de Voort et al. 2019; Ramesh & Nelson 2024). Several studies have made comparisons of hydrodynamical simulations from the CGM scale to the ICM scale (Lim et al. 2021; Lee et al. 2022; Yang et al. 2022). More recently, using Cosmology and Astrophysics with MachinE Learning Simulations (CAMELS) simulations with varying feedback parameters in a variety of subgrid physics modules (Villaescusa-Navarro et al. 2021; Ni et al. 2023; Lee et al. 2024), it has become possible to systematically explore the impact of feedback physics on CGM observables, such as the tSZ effect (Moser et al. 2022), X-ray (Butler Contreras et al. 2023), and FRB (Medlock et al. 2024).

Understanding how feedback impacts the CGM observables is complex because of the interplay of physical processes in hydrodynamical simulations. Exploring the parameter spaces of feedback physics using these simulations is also computationally expensive. Idealized analytical CGM models, on the other hand, can efficiently isolate the impact of specific physical processes. Therefore, both idealized models and hydrodynamical simulations are crucial for accurately modelling gas physics and improving our understanding of CGM and its role in galaxy evolution. Comparison of different CGM models in the literature can be challenging because they are based on different input assumptions, such as the underlying dispersion measure (DM) halo potential, models of gas cooling, and metal distributions.

In this study, we compare four idealized Milky Way-like CGM models that represent different key aspects of CGM physics. The goal is to determine whether upcoming multiwavelength observations can differentiate between these models. The models being compared are the precipitation model (Voit et al. 2018, 2019; Singh et al. 2021), isentropic model (Faerman et al. 2020, 2022), cooling flow model (Stern et al. 2019, 2020, 2023), and the baryon pasting model (Shaw et al. 2010; Flender, Nagai & McDonald 2017; Osato & Nagai 2022). To facilitate an efficient and meaningful comparison between these different CGM models, we have developed a standardized Python pipeline to input the models and compute observables consistently. Our main objectives are to: (i) compare different CGM models in a standardized manner, (ii) highlight inherent differences arising from the different implementations of physical processes governing CGM physics, and (iii) provide the scientific community with a user-friendly pipeline that can be expanded to include additional models.

The organization of the paper is as follows: Section 2 briefly introduces the conservation equations of mass, momentum, and energy that govern CGM thermodynamics and the four idealized CGM models that we address. In Section 3, we compare the entropy, pressure, density, and temperature profiles for the fiducial parameter

values of these CGM models. Section 4 describes the observational predictions, such as SZ, X-ray surface brightness, oxygen column densities, and dispersion measure profiles. We summarize the results of our analysis in Section 5.

# 2 IDEALIZED ONE-DIMENSIONAL MODELS OF THE CGM

#### 2.1 General framework

For the hot, diffuse CGM, we can reasonably assume that the gas is collisional with low viscosity, given that the mean free path is small for the weakly magnetized plasma. The thermodynamical properties of a collisional inviscid fluid in a gravitational potential can generally be described by the three equations that represent the conservation of mass, momentum, and energy (or entropy).

The one-dimensional radial equations for mass and momentum conservation for the inviscid CGM are,

$$\frac{\partial \rho}{\partial t} + \frac{\partial}{\partial \mathbf{r}} (\rho \, v_{\mathbf{r}}) = 0, \tag{1}$$

$$\frac{\partial v_{\rm r}}{\partial t} + v_{\rm r} \frac{\partial v_{\rm r}}{\partial \rm r} = -\sum_{i} \frac{1}{\rho} \frac{\partial P_{i}}{\partial \rm r} - \frac{\partial \Phi}{\partial \rm r}, \tag{2}$$

where  $\rho$  is gas density,  $v_r$  is the radial velocity component,  $P_i$  is  $i^{th}$  gas pressure component, and  $\Phi$  is the gravitational potential. The specific angular momentum is assumed to be zero for the CGM models considered in this paper. The total gas pressure can be written as the sum of contributions from thermal pressure, turbulence, magnetic fields, and cosmic rays (i.e.  $P = \sum_i P_i = P_{th} + P_{turb} + P_B + P_{CR}$ ), where different pressure components correspond to different polytropic indices,  $\gamma_i$ .

The one-dimensional energy conservation equation, again assuming negligible thermal conduction and viscosity, is expressed as:

$$\frac{\partial}{\partial t} \left[ \rho \left( e + \frac{v_{\rm r}^2}{2} \right) \right] + \frac{\partial}{\partial r} \left[ \rho \left( e + \frac{v_{\rm r}^2}{2} \right) v_{\rm r} + P v_{\rm r} \right] 
= -\rho v_{\rm r} \frac{\partial \Phi}{\partial r} + \mathcal{H} - \mathcal{C},$$
(3)

where e is the velocity dispersion,  $\mathcal{H}$  and  $\mathcal{C}$  represent the non-adiabatic heating and cooling per unit volume, respectively: heating occurs at the accretion shock at the outer boundary of the halo, at merger shocks, as well as through feedback at the halo core and through turbulent dissipation throughout the volume of the halo. Cooling is mainly driven by metallicity-dependent radiative cooling. Alternatively, equation (3) can be rewritten as the conservation of entropy  $K \equiv P \rho^{-\gamma}$ :

$$\left(\frac{P}{\gamma - 1}\right) \frac{\partial \ln K}{\partial t} + v_{\rm r} \left(\frac{P}{\gamma - 1}\right) \frac{\partial \ln K}{\partial r} = \mathcal{H} - \mathcal{C},\tag{4}$$

The equations described above govern the thermodynamics and kinematics of the CGM, and can be reduced to simpler forms under certain assumptions about the CGM properties. We now discuss these for different models.

## 2.2 Precipitation model

The precipitation-limited hot halo model (simply precipitation model henceforth) (Sharma et al. 2012, Voit et al. 2018, 2019; Singh et al. 2021) assumes the halo gas is in hydrostatic equilibrium, with no large-scale ordered inflows or outflows, i.e.  $v_r \approx 0$  in equations (1) and (2), setting the components on the left-hand side of equation (2)

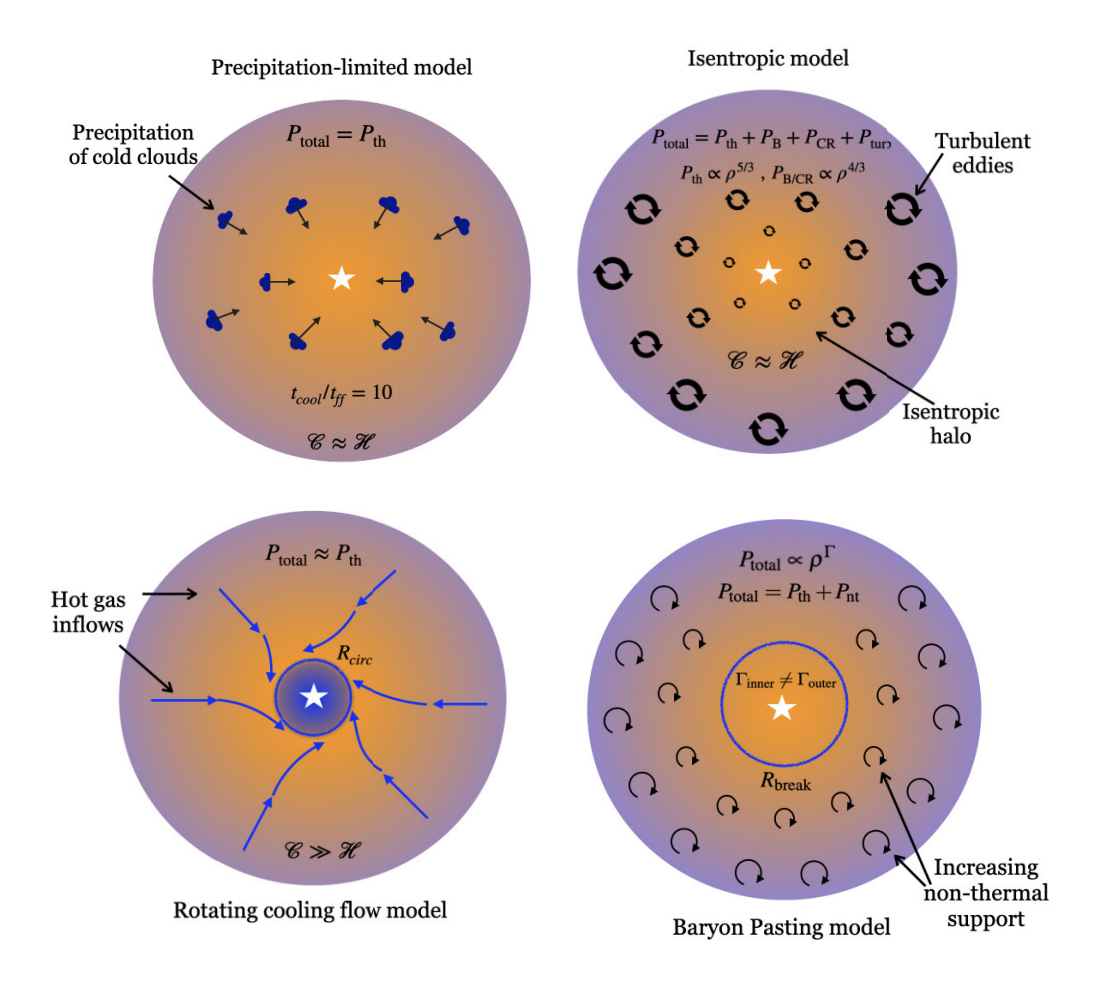


Figure 1. An illustration of the idealized CGM models considered in this work. Orange indicates a higher gas temperature than blue. Top-left (precipitation model): Thermal balance ( $\mathcal{C} \approx \mathcal{H}$ ) is maintained while the ratio  $t_{\text{cool}}/t_{\text{ff}}$  is fixed above a critical value of 10 throughout the halo. In cases where  $t_{\text{cool}}/t_{\text{ff}} < 10$ , precipitation of cold clouds on to the central galaxy fuelling star formation and central supermassive black hole takes place. This is followed by feedback processes, which regulate the system back to thermal balance. Top-right (isentropic model): The thermal balance is maintained throughout the halo. The nonthermal contribution to the total pressure increases with increasing galactocentric radii. Among the non-thermal components, the relative fraction of turbulent support increases faster. Bottom-left (cooling flow model): Cooling dominates non-adiabatic heating throughout the halo. A hot inflow develops down to the circularization radius Rcirc, at which the hot inflow cools and fuels star formation. Bottom-right (baryon pasting model): The relation between CGM pressure and density is controlled by a polytropic index  $\Gamma$ . The impact of the cooling core is captured by a break in the value of  $\Gamma$  at  $R_{\text{break}}$ , where  $\Gamma_{\text{inner}} \ll \Gamma_{\text{outer}}$ . The non-thermal pressure increases with increasing galactocentric radii.

to zero. The key ingredient of the precipitation model is a fixed ratio of gas cooling to free-fall time-scales  $(t_{cool}/t_{ff})$  throughout the halo, where  $t_{\rm ff} = \sqrt{2} \times r/v_{\rm c}$  is the free-fall time,  $v_{\rm c} = \sqrt{GM(< r)/r}$  is the circular velocity, and  $t_{\text{cool}} \equiv (\gamma - 1)^{-1} P_{\text{th}} / \mathcal{C}$  is the cooling time.

The entropy profile of the precipitation model is a sum of two components, a baseline entropy profile  $(K_{base})$  and a precipitation limited entropy profile  $(K_{pre})$  given by

$$K_{\text{base}}(r) = 1.32 \frac{kT_{\phi}(R_{200})}{\bar{n}_{\text{e},200}^{2/3}} \left(\frac{r}{R_{200}}\right)^{1.1}, \tag{5}$$

$$K_{\text{pre}}(r) = (2\mu m_{\text{p}})^{1/3} \left[ \left(\frac{t_{\text{cool}}}{t_{\text{ff}}}\right) \frac{2n_{i}}{n} \frac{\Lambda(2T_{\phi}, Z)}{3} \right]^{2/3} r^{2/3} . \tag{6}$$

$$K_{\text{pre}}(r) = (2\mu m_{\text{p}})^{1/3} \left[ \left( \frac{t_{\text{cool}}}{t_{\text{fr}}} \right) \frac{2n_i}{n} \frac{\Lambda(2T_{\phi}, Z)}{3} \right]^{2/3} r^{2/3}$$
 (6)

Here,  $T_{\phi}$  is the gravitational temperature of the halo  $(kT_{\phi} \equiv$  $\mu m_p v_c^2(r)/2$ ,  $\bar{n}_{e,200}$  is the mean electron density corresponding to 200 times the critical density, and  $\Lambda(T, Z) = C/n_H^2$  is the cooling function which depends on gas temperature and metallicity.

The baseline entropy profile in equation (5) is a fit to simulated clusters from gravity-only cosmological simulations in the radial range  $(0.2 - 1) \times R_{200}$  (Voit 2005). It represents the non-adiabatic

gravitational heating from accretion shocks  $\mathcal{H}$  in equation (4). The value of  $t_{\rm cool}/t_{\rm ff}$  controls the precipitation-limited entropy profile in equation (6), constraining the metallicity-dependent gas cooling  $\mathcal{C}$  in equation (4). The precipitation model also considers only the contribution to the gas pressure of the thermal component. Fig. 1 (top left) illustrates a thermal balance when condition  $t_{\rm cool}/t_{\rm ff} \gtrsim 10$ is satisfied. The precipitation of cold clouds on to the central galaxy follows as  $t_{\rm cool}/t_{\rm ff}$  falls below this critical value. Precipitation, in turn, fuels next-generation feedback processes, thus restoring the system to thermal balance.

In summary, the precipitation model attempts to portray a picture of a gaseous halo in hydrostatic equilibrium with its host halo, while gas hydrodynamics on global scales is mainly governed by the ratio of  $t_{cool}$  and  $t_{ff}$ . It provides an upper limit on the gas density, which then translates to the upper limit on the observed X-ray luminosity temperature relation (Voit et al. 2018) from individual galaxies to massive galaxy clusters, i.e. three orders of magnitudes in halo masses ( $\sim 10^{12}$ – $10^{15}\,\mathrm{M}_{\odot}$ ). The observed precipitation limit corresponds to a lower limit on  $t_{\rm cool}/t_{\rm ff} \sim 10$ .

# 2.3 Isentropic model

The isentropic model, presented in Faerman et al. (2020, hereafter FSM20), describes a large-scale, spherically symmetric corona, with gas in hydrostatic equilibrium in the gravitational potential of an MW mass dark matter halo. The model is motivated by galactic feedback heating, from active galactic nuclei (AGN) or star formation, leading the CGM to evolve toward marginal convective equilibrium. The model, therefore, adopts an adiabatic equation of state (EoS),  $P = K \rho^{\gamma}$ , where K is the entropy parameter, constant with radius. The model allows for three pressure components: (i) thermal, (ii) non-thermal from magnetic fields and cosmic rays (B/CR), and (iii) turbulent support. Polytropic indices are  $\gamma_1 = 5/3$  for the thermal pressure and  $\gamma_2 = 4/3$  for the B/CR component, modelled as a relativistic fluid. The model assumes a constant velocity scale for the turbulent component,  $\sigma_{\text{turb}}$ , corresponding to  $\gamma_3 = 1$ .

The model assumes that there are no large-scale ordered inflows or outflows ( $v_r \approx 0$  in equations 1 and 2). Equation (2) can then be written as,

$$\left(\sigma_{\text{turb}}^2 + \sum_{i=1,2} \gamma_i K_i \rho^{\gamma_i - 1}\right) \rho^{-1} d\rho = -\frac{GM(r) dr}{r^2} \quad . \tag{7}$$

 $K_i$  are constant with radius and are calculated at the boundary as functions of the gas properties – the temperature,  $T_{\text{th,b}}$ , density,  $\rho_{\text{b}}$  and amount of non-thermal support. The latter is parametrized in Faerman et al. (2017) as  $\alpha \equiv (P_{\text{th}} + P_{\text{nth}})/P_{\text{th}} = (T_{\text{th}} + T_{\text{nth}})/T_{\text{th}}$ . The entropy parameters are then given by

$$K_{1} = \frac{k_{\rm B}}{\bar{m}^{\gamma_{1}}} \frac{T_{\rm th,b}}{n_{\rm b}^{\gamma_{1}-1}} , \quad K_{2} = \frac{k_{\rm B}}{\bar{m}^{\gamma_{2}}} \frac{(\alpha_{\rm b} - 1)T_{\rm th,b}}{n_{\rm b}^{\gamma_{2}-1}} , \tag{8}$$

where  $\alpha_b \equiv \alpha(r_{\text{CGM}})$ . Fig. 1 (top-right) illustrates the rapidly decreasing gas temperature and increasing non-thermal contribution to total pressure (from turbulence, magnetic fields, and cosmic rays) with increasing galactocentric radius in the isentropic model.

To summarize, the model's input parameters are the gas density, temperature, ratio of non-thermal to thermal pressure at the halo boundary, and the turbulent velocity in the CGM. Setting these allows us to solve equation (7) for the gas density profile,  $\rho(r)$ , and then use the constant-entropy EoS (a solution to equation 4) to find the pressure profiles for each of the components.

In FSM20, the CGM metallicity varies with the distance from the galaxy, and the gas ionization state is set by collisional ionization and photoionization by the (redshift-dependent) metagalactic radiation field (Haardt & Madau 2012; Ferland et al. 2017). In this work, to compare with other CGM models, we set the metallicity in the isentropic model to be constant with radius and assume only collisional ionization equilibrium.

Given the distribution of gas and metals and the gas cooling function, the model calculates the radiative cooling luminosity of the CGM. These radiative losses can be translated to the mass cooling rate as a function of radius and integrated to give the global cooling rates for the entire corona. The model assumes that, on average, the CGM is in equilibrium, and these losses are balanced by energy inputs from processes such as galactic feedback, accretion, dissipation of turbulence, etc., or mass inputs from accretion and galactic outflows. This balance does not have to be perfect for star-forming galaxies

and on short time-scales, allowing for cooling–heating or accretion-outflow cycles (see the discussion in Faerman et al. 2022). In summary, the model requires a time-averaged net heating–cooling balance with star formation (i.e.  $\langle \mathcal{C} - \mathcal{H} \rangle \propto \langle \text{SFR} \rangle$ ). Faerman & Werk (2023) extend this model by adding a cool gas phase, in heating/cooling and ionization equilibrium with the metagalactic radiation field, formed by precipitation from the hot phase, accreted from the intergalactic medium, stripped from satellites, or ejected from the galaxy.

#### 2.4 Cooling flow model

The cooling flow model discussed in Stern et al. (2019) assumes that the dynamical and heating effects of feedback on the CGM are small during the last cooling time-scale  $t_{\rm cool}$ . This assumption is expected to be valid either if feedback occurs in bursts that are separated by more than  $t_{\rm cool}$  or in low-redshift galaxies in which the effect of feedback heating on the CGM was strong at high redshift and has since subsided. This assumption is also more easily satisfied at small CGM radii, where  $t_{\rm cool}$  is a few  $100\,{\rm Myr}-1\,{\rm Gyr}$ , in contrast to large CGM radii where  $t_{\rm cool}$  can reach a Hubble time. It is thus plausible that the CGM forms a cooling flow at small radii where  $t_{\rm cool}$  is sufficiently short, while at large radii, the CGM more resembles the 'thermal balance' models considered above.

At radii where the cooling flow assumption is satisfied, equation (4) implies,

$$\frac{\mathrm{d}\ln K}{\mathrm{d}r} = -\left[v_{\mathrm{r}}\left(\frac{P_{\mathrm{th}}}{\gamma_{\mathrm{th}} - 1}\right)\right]^{-1} \mathcal{C} = -\frac{1}{v_{\mathrm{r}}t_{\mathrm{cool}}}$$
(9)

where for simplicity we assumed  $P_{\rm B} = P_{\rm CR} = P_{\rm turb} = 0$ , and we used the definition of the cooling time  $t_{\rm cool} \equiv (\gamma - 1)^{-1} P_{\rm th}/\mathcal{C}$ . The model is illustrated in the bottom-left of Fig. 1. Note that despite the name 'cooling flows', the inflowing gas remains hot down to the galaxy scale, since radiative losses are compensated by compressive heating.

In the limits  $t_{\rm cool}^2 \gg t_{\rm ff}^2$  (as expected in  $M_{\rm vir} \gtrsim 10^{12} \, {\rm M}_{\odot}$  haloes) and  $\mathcal{C} \gg \mathcal{H}$ , analytic calculations and hydrodynamic simulations demonstrate that the CGM converges on a specific solution to equations (1)–(4) in which

$$\frac{\mathrm{d}\ln K}{\mathrm{d}\ln r} = \frac{r/v_{\rm r}}{t_{\rm cool}} \approx 1 + \frac{4}{3}m\tag{10}$$

where,  $m \equiv \operatorname{d} \ln v_{\rm c}/\operatorname{d} \ln r$ , and the approximation is exact for a power-law potential of the form  $v_{\rm c} \propto r^m$ . For an isothermal potential m=0, therefore, we get  $K \propto r$ . Also, since  $v_{\rm r} \approx r/t_{\rm cool}$ , we see that the ratio of the inertial term to the gravitational term in equation (2) is of the order  $(v_{\rm r}/v_{\rm c})^2 \approx (t_{\rm cool}/t_{\rm ff})^{-2} \ll 1$ , and hence a cooling flow is similar to the hydrostatic models considered above, with small deviations from hydrostatic equilibrium of the order  $(t_{\rm cool}/t_{\rm ff})^{-2}$ .

At small radii, centrifugal forces induced by angular momentum will change the structure of the hot gas and break its spherical symmetry. The implied axisymmetric solution was recently derived for the cooling flow model by Stern et al. (2023), who showed that rotational support induces deviations from the hydrostatic equilibrium of order  $(r/R_{\rm circ})^{-2}$ , where the circularization radius  $R_{\rm circ}$  is defined through  $j=v_{\rm c}(R_{\rm circ})R_{\rm circ}$  and depends on the spin of the inflowing hot gas. For MW-like haloes, we expect  $R_{\rm circ}\approx 15$  kpc. At  $r\leq R_{\rm circ}$ , angular momentum support causes the hot inflow to halt, flatten into a disc geometry, cool and from  $\sim 10^6$  to  $\sim 10^4$  K at the disc–halo interface. We discuss the implications of angular momentum on our results in Section 3.

 $<sup>^{1}\</sup>alpha$  is constant with radius for an isothermal gas distribution. In FSM20, the relative fractions of pressure support of each component vary with radius, and  $\alpha$  is not constant.

3226 *P. Singh et al.* 

**Table 1.** A summary of the four CGM models. Here  $t_{\text{cool}}$  is gas cooling time-scale,  $t_{\text{ff}}$  is free-fall time-scale, and  $M_{\text{CGM}}$  is the CGM mass.

|                       | Precipitation  | Isentropic  | Cooling flow   | Baryon pasting  |
|-----------------------|--|---|--|---|
| Momentum conservation | Hydrostatic equilibrium                              | Hydrostatic equilibrium                               | Hydrostatic equilibrium up to $(t_{\text{cool}}/t_{\text{ff}})^{-2}$ | Hydrostatic equilibrium   |
| Functional constraint | Radially independent $t_{\text{cool}}/t_{\text{ff}}$ | Constant entropy                                      | Energy + mass conservation in hot inflow                             | Polytropic relation   |
| Boundary condition    | Gas temperature at outer boundary                    | Gas temperature at outer boundary                     | Gas temperature at outer boundary and SFR (or $M_{CGM}$ )            | Confining pressure  |
| Dynamical support     | None   | Constant turbulent velocity dispersion                | Small, of order $(t_{\rm cool}/t_{\rm ff})^{-2}$                     | Non-thermal pressure profile as parametric model with free parameters |
| Other support         | None   | Magnetic fields + cosmic rays as a relativistic fluid | None   | None  |

# 2.5 Baryon pasting model

The Baryon Pasting (BP) model is an analytic model of halo gas initially developed for galaxy clusters. It models gas with a polytropic equation of state, where the pressure of the gas is related to its density, including essential physics such as cooling, star formation, and feedback (Ostriker, Bode & Babul 2005), non-thermal pressure due to bulk and turbulent gas motions (Shaw et al. 2010), cool-core (Flender et al. 2017), and gas density clumping (Shirasaki, Lau & Nagai 2020). The latest BP model also features the painting of gas on DM particle in *N*-body simulation, in addition to painting gas on DM halo (Osato & Nagai 2022).

The BP model assumes that the total pressure  $P_{\text{tot}}$  (thermal + non-thermal) of the halo gas is in hydrostatic equilibrium with the gravitational potential of the DM halo. The total pressure is related to the gas density through the polytropic relation:

$$P_{\text{tot}}(r) = P_0 \theta(r)^{n+1}, \tag{11}$$

where the gas density is given by  $\rho_{\rm g}(r)=\rho_0\theta(r)^n$ ,  $\theta(r)=1+\frac{\Gamma-1}{\Gamma}\frac{\rho_0}{P_0}(\Phi_0-\Phi(r))$  is a dimensionless function that represents the gas temperature,  $\Phi_0$  is the central potential of the halo, and  $\Gamma=1+1/n$  is the polytropic exponent, a parameter in the BP model. We set  $\Gamma=1.2$  outside cluster cores  $(r>0.2R_{500c})$  as suggested from both cosmological hydrodynamical simulations and observations (see e.g. Voit 2005). Within the core  $(r<0.2R_{500c})$ , by  $R_{\rm break}$  in the bottomright panel of Fig. 1), the polytropic equation of state is modelled as  $\Gamma_{\rm mod}=\Gamma_{\rm mod},0(1+z)^\beta$ , including the dependence on redshifts.

The normalization constants of the pressure and gas density profile,  $P_0$  and  $\rho_0$ , respectively, are determined numerically by solving the energy and momentum conservation equations. In particular, the energy of the gas is given by

$$E_{g,f} = E_{g,i} + \epsilon_{DM} |E_{DM}| + \epsilon_f M_{\star} c^2 + \Delta E_p. \tag{12}$$

where  $E_{\rm g,f}$  and  $E_{\rm g,i}$  are the final and initial total (the sum of kinetic, thermal, and potential) energies of the gas.  $\Delta E_{\rm p}$  is the work done by the gas as it expands.  $\epsilon_{\rm DM}|E_{\rm DM}|$  is the energy transferred to the gas during major halo mergers through dynamical friction. The term  $\epsilon_{\rm f} M_{\star} c^2$  is the energy injected into the gas due to feedback from both supernovae (SNe) and AGN, and  $M_{\star}$  is the total stellar mass. The slope and normalization of the stellar mass—halo mass relation are two of the model's free parameters. Note that these two constraint equations are re-expressions of the conservation equations (equations 1, 2, and 4).

The baryon pasting model includes the effects of non-thermal pressure in the gas by adopting the 'universal' non-thermal pressure fraction profile (Nelson, Lau & Nagai 2014). The non-thermal pressure fraction is defined as  $P_{\rm nt} = P_{\rm tot}(1-f_{\rm th})$ . The free parameters of the model are calibrated with the density profiles of the *Chandra*-SPT sample, covering a mass-limited cluster sample with  $M_{500c} \geq 3 \times 10^{14} {\rm M}_{\odot}$  for redshift up to z=1.7, as well as the gas mass and total mass relations in clusters and groups from the *Chandra* and *XMM-Newton* data (see Section 3 and table 3 of Flender et al. 2017 for the details of the model parameters and their fiducial values).

Note that the baryon basting model used here is an updated version of Flender et al. 2017. Instead of setting the pressure boundary to be the virial radius, the updated model uses  $R_{200\text{m}}$ . This radius is a better match to the splash-back radius, which is closer to a physical boundary of the halo gas than the virial radius (e.g. Shi 2016; Aung, Nagai & Lau 2021).

We have built a Python pipeline (https://github.com/psingh220/scam\_cgm) to systematically compare different analytical CGM models. This pipeline allows for a fair comparison by properly assessing the quantities that are used in the predictions of the models. The CGM modelling interface provides a common platform for inputting parameters such as halo potential, metallicity profile, cooling function, boundary conditions, and model-specific parameters into individual CGM models. We will now present the output of our pipeline.

### 3 THERMODYNAMIC PROFILES OF THE CGM

Table 1 summarizes the modelling assumptions for the four models presented in Section 2. The conservation of momentum is reduced to hydrostatic equilibrium in all four CGM models (in a cooling flow, hydrostatic equilibrium holds up to deviations of the order  $t_{\rm cool}^2/t_{\rm ff}^2$ ). The functional constraint signifies where the models' assumptions about CGM properties differ while solving Euler's equations. The isentropic and baryon pasting models include additional non-thermal pressure support in equations (2) and (4) through turbulence, magnetic fields, and cosmic rays.

In Fig. 2, we compare the gas entropy, thermal pressure, electron density, and temperature profiles for the four CGM models. The presented thermodynamic profiles are derived for a halo mass  $M_{\rm vir}=10^{12}~{\rm M}_{\odot}$  at redshift  $z\sim0$ , in an Navarro–Frenk–White (NFW) + galaxy potential with concentration  $c_{\rm vir}=10,~M_*=6\times10^{10}~{\rm M}_{\odot}$ , and a galactic disc scale length of 2.5 kpc. The cooling function is calculated using the CLOUDY 17.00 (Ferland et al. 2017) tables under collisional ionization equilibrium (CIE) for uniform metallicity. For simplicity, we fix the CGM metallicity to 0.3  $Z_{\odot}$ .

<sup>&</sup>lt;sup>2</sup>The exact value of  $\epsilon_{DM}$  remains uncertain and is likely to depend on other factors, such as the merger history of a given halo.

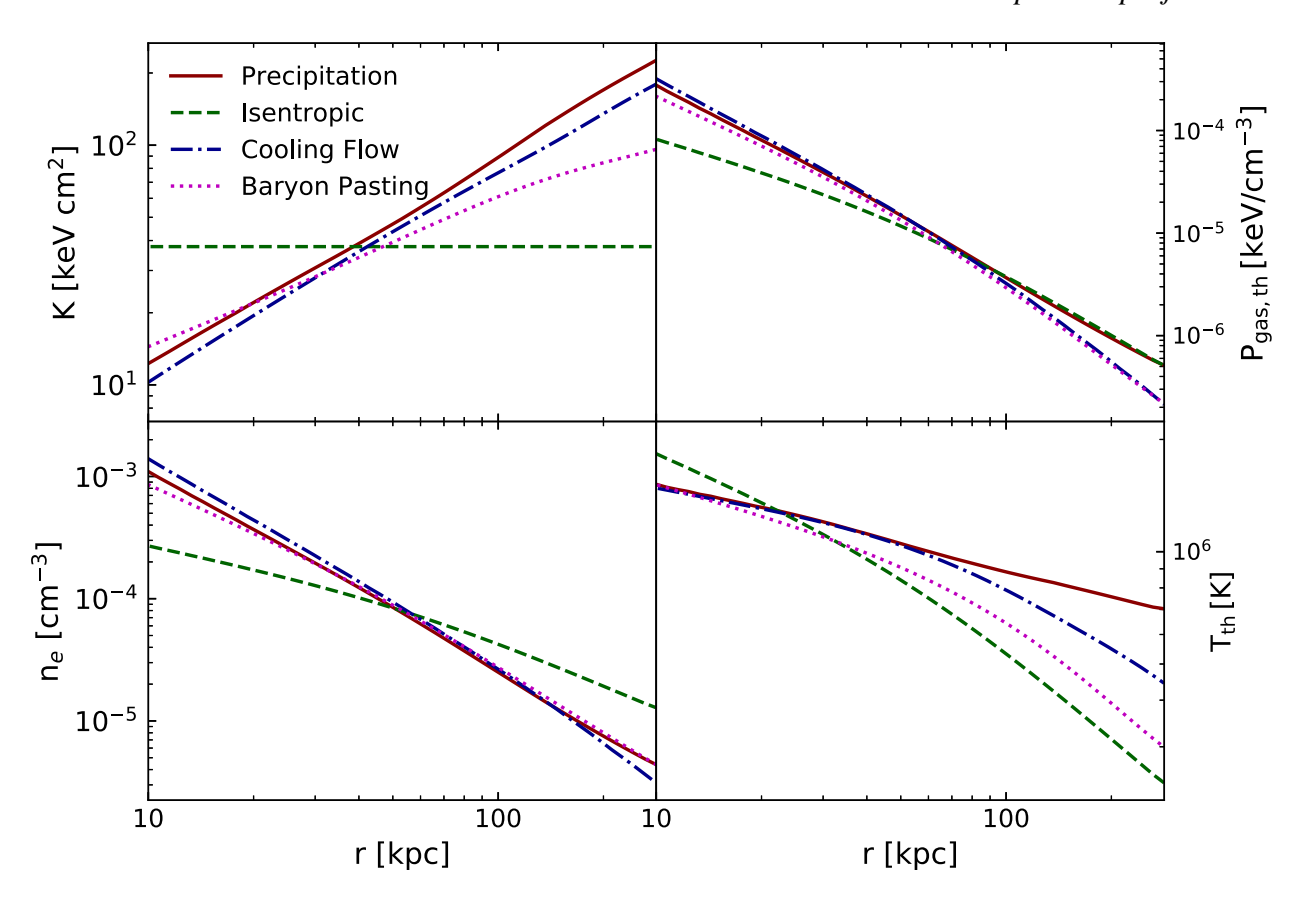


Figure 2. Specific entropy (top-left panel), thermal gas pressure (top-right panel), electron density (bottom left-hand panel), and temperature (bottom-right panel) profiles for a halo with  $M_{\rm vir} \sim 10^{12}~{\rm M_{\odot}}$  at  $z \sim 0$ , for the precipitation (solid red), isentropic (dashed green), cooling flow (dashed–dotted blue), and baryon pasting (dotted magenta) models. Additional details on input quantities and fiducial model parameters are presented in Table 2 and Section 3.

Table 2. Common input parameters to the CGM models.

| $M_{ m vir}$            | $10^{12}~{ m M}_{\odot}$               |  |  |
|-------------------------|--|--|--|
| z.                      | 0.001                                  |  |  |
| Gravitational potential | NFW + galaxy with                      |  |  |
|                         | concentration $c_{\rm vir} = 10$       |  |  |
| $M_*$                   | $6 	imes 10^{10} \ \mathrm{M}_{\odot}$ |  |  |
| Disc scale length       | 2.5 kpc                                |  |  |
| Metallicity             | $0.3  \mathrm{Z}_{\odot}$ (uniform)    |  |  |
| Ionization & cooling    | Collisional ionization equilibrium     |  |  |
| Outer boundary          | 280 kpc                                |  |  |

The boundary conditions are provided at 280 kpc (close to the virial radius) except for the baryon pasting model where it is 365 kpc (i.e.  $R_{200m}$ ).

Thermodynamic profiles for the precipitation model are shown for  $t_{\rm cool}/t_{\rm ff}=10$  and gas temperature  $\sim 0.06\,{\rm keV}~(\approx 7\times 10^5\,{\rm K})$  at the boundary. The isentropic model profiles are shown for the fiducial model from FSM20, with  $T_{\rm b}=2.4\times 10^5\,{\rm K}$  and  $n_{\rm b}=10^{-5}\,{\rm cm}^{-3}$  (see Table 1). For the cooling flow model, we show a 1D non-rotating solution with mass inflow rate  $\dot{M}=1\,{\rm M}_{\odot}\,{\rm yr}^{-1}$ . Table 2 summarizes the common input parameters of the models.

We note that angular momentum is expected to cause significant deviations from spherical symmetry at radii  $\lesssim R_{\rm circ} \sim 15\,{\rm kpc}$ . Specifically in the cooling flow solution, Stern et al. (2023) showed that this results in higher densities and lower temperatures in the disc plane versus the rotation axis and the spherically symmetric solution

shown in Fig. 2. The deviations scale as  $(r/R_{cire})^{-2}$ , i.e. they become rapidly stronger with decreasing radius.

The slopes of the thermodynamic profiles in the isentropic model are considerably different from those of the other models. The gas temperature in the isentropic model is notably lower at  $r\gtrsim 30\,\mathrm{kpc}$  due to the lower boundary temperature adopted and the presence of non-thermal pressure support. The latter also results in a shallower density profile, leading to lower gas densities in the central region and higher densities at large radii. The fiducial precipitation and cooling flow models show similar thermodynamic profiles at  $r\lesssim 100\,\mathrm{kpc}$ . At larger radii, they differ in gas temperature and pressure, though at these large radii,  $t_{\rm cool}$  approaches the Hubble time, so it is not clear that a cooling flow has time to develop.

For the baryon pasting model, the profiles shown are for the best-fitting parameters fitted to the cluster and group X-ray observations from table 3 of Flender et al. (2017) except for the feedback efficiency. The feedback energy from SN and AGN per stellar mass,  $\epsilon_{\rm f} = E_{\rm feedback}/(M_{\star}c^2)$ , which is set in this work to  $10^{-6}$ , a factor of four lower than the fiducial value,  $\epsilon_{\rm f} = 4 \times 10^{-6}$ , which was calibrated from galaxy cluster observations. The higher feedback efficiency and, hence, the higher feedback energy that better describes ICM pushes more CGM outside the potential well. It also heats the gas to a higher temperature. This leads to a density and pressure that are more than an order of magnitude lower and a higher temperature for the baryon pasting model than other CGM models. Lowering the feedback efficiency to  $10^{-6}$  brings the BP model into a much better agreement with the other CGM models. If the model is accurate, this suggests that the CGM favours a lower feedback

3228

efficiency than the ICM. This is consistent with the scenario in which SN feedback alone can provide enough energy to lift the CGM gas from the bottom of the potential well. However, agreement with other models alone does not mean that the real CGM prefers a lower feedback efficiency. For example, recent ACT SZ measurements of gas profiles of stacked massive galaxies and groups (Amodeo et al. 2021) prefer higher feedback efficiencies. These observations suggest much higher thermal pressure and density profiles than state-of-the-art simulations.

The slope of the entropy profiles is  $\sim 0.8 - 0.9$  for the precipitation and cooling flow models,  $\sim 0.6$  for the baryon pasting model, and 0 (by construction) for the isentropic model. As noted earlier, the cooling flow and precipitation can be differentiated using a higher gas temperature at large galactocentric distances. Therefore, the combination of entropy and temperature profiles is the best discriminator among these models. Observational probes (or their combinations) that directly probe the entropy profile can be used to test the isentropic model. Precipitation-regulated gaseous haloes have a distinctively higher entropy and temperature at the galaxy outskirts. Cooling flows lead to the steepest entropy, density, and pressure profiles. Consequently, we need radially resolved profiles and probes sensitive to large galactocentric distances to discern the dominant physical processes shaping the global properties of the CGM, and we now present predictions for some key observational probes.

#### 4 CGM OBSERVABLES

In this section, we calculate the SZ effect, soft X-ray emission, FRB dispersion measure, and column densities of O VI, O VII, and O VIII, measurable in absorption, for the fiducial models described in Section 3. All these quantities are calculated and plotted for an external observer looking through the CGM.

# 4.1 Sunyaev-Zeldovich effect

SZ effect is a secondary distortion in the blackbody spectrum of the CMB through inverse Compton scattering of low-energy CMB photons with high-energy electrons present in the intervening ionized gaseous medium (Sunyaev & Zeldovich 1972). The tSZ effect traces the thermal gas pressure and is characterized by a dimensionless *y*-parameter defined as:

$$y_{\rm tSZ} = \frac{\sigma_{\rm T}}{m_{\rm e}c^2} \int P_{\rm e} \, \mathrm{dl},\tag{13}$$

where  $\sigma_T$  is the Thompson scattering cross-section,  $P_e$  is the electron pressure, and integration is performed along the line of sight. The change in CMB temperature due to the tSZ effect is a multiplication of the y-parameter and its unique frequency dependence. The kinetic SZ (kSZ) effect could be used to constrain the gas density modulo the line-of-sight bulk gas velocity and is directly given by the decrement caused by it in the CMB temperature.

$$T_{\rm kSZ} = -T_{\rm CMB} \frac{\sigma_T}{c} \int n_{\rm e} v_{\rm los} \, {\rm dl}, \tag{14}$$

where  $n_{\rm e}$  is the electron density,  $v_{\rm los}$  is the line-of-sight velocity of the medium away from us, and  $T_{\rm CMB}$  is the temperature of the undistorted CMB.

In the top left-hand panel of Fig. 3, we show the projected *y*-parameter profiles due to the tSZ effect (or simply the tSZ profiles) for the four fiducial CGM models. The precipitation, cooling flow, and baryon pasting models predict very similar tSZ profiles at

small scales ( $r < 50 \,\mathrm{kpc}$ , although note the angular momentum effects for the cooling flow model discussed above). In contrast, the precipitation and isentropic models converge at galaxy outskirts, tracing their pressure profiles. The cooling-flow and baryon pasting models predict a comparatively steeper, and the isentropic model predicts a shallower tSZ profile. The fiducial model predictions differ by a maximum factor of two near the galaxy centre and outskirt, while converging at intermediate scales. These results indicate the need for higher-angular-resolution CMB experiments probing smaller scales to use the tSZ signal to differentiate the CGM models.

Stage-3 (AdvACT and SPT-3G) and Stage-4 (CMB-S4) CMB surveys will play a critical role in resolving SZ profiles with high signal-to-noise ratio, providing the opportunity to constrain CGM physics down to  $10^{12}~M_{\odot}$  (Battaglia et al. 2019). The dotted line and arrows show the expected sensitivity limit  $\sim 10^{-9}$  for CMB-S4 at 150~GHz (assuming the noise RMS of  $1.8~\mu K$ -arcmin, see table 1 of Battaglia et al. 2017) for a stack of  $\approx 300~000$  galaxies. The same frequency channel is expected to have an angular resolution of  $\sim 1~arcmin$ , corresponding to a spatial resolution of 50-100~kpc for a median redshift of  $\sim 0.05-0.1$ . Combining several frequency channels would significantly improve the sensitivity limit, at the cost of lower angular resolution.

We show the kSZ profile predictions in the bottom-left panel (right y-axis), assuming a typical peculiar velocity of 300 km s<sup>-1</sup> (Schaan et al. 2021; Tanimura et al. 2022). The shape of the kSZ profile is identical to the FRB dispersion measure profile (Section 4.3 below) since both observables trace the electron density integrated along the line of sight.<sup>3</sup> Note that the change in CMB temperature induced by the kSZ signal is larger than that of the tSZ signal (=  $y_{\text{tSZ}}T_{\text{CMB}}$ ) throughout an  $M_{\text{vir}} \sim 10^{12} \text{ M}_{\odot}$  halo, in contrast to galaxy clusters ( $M_{\text{vir}} \sim 10^{15} \text{ M}_{\odot}$ ) where the tSZ signal dominates due to the higher ICM temperature. The ratio of kSZ to tSZ decrements is lowest in the precipitation model (kSZ/tSZ  $\sim$  3 and increases with increasing distance from the centre) in the low-frequency limit (where the tSZ frequency-dependent factor  $\approx$  -2). The ratio increases to  $\sim$  5 for the cooling flow and to  $\sim$  10 for the BP and isentropic models.

The kSZ sensitivity limit of CMB-S4 at 150 GHz is an order of magnitude above the predictions for the four fiducial models. Assuming that an accurate galaxy peculiar velocity estimation can be obtained with an overlapping spectroscopic survey like Dark Energy Spectroscopic Instrument (DESI; Ried Guachalla et al. 2023), a sensitivity of  $\sim 5\times 10^{-3}~\mu K$  can be achieved by stacking  $\sim 100\,000$  galaxies. Such sensitivity levels are sufficient to detect the kSZ signal out to the virial radius for our fiducial models. Therefore, extracting accurate galaxy peculiar velocities poses both a challenge and an exciting avenue for studying the CGM in  $L_*$  galaxies with the kSZ effect in future CMB surveys and advanced techniques.

### 4.2 Soft X-ray emission

Detection of extended X-ray emission from nearby galaxies is one of the few direct observations of hot CGM (Anderson & Bregman 2011; Anderson et al. 2016; Bogdán et al. 2017; Li et al. 2018, Das et al. 2019b, Das et al. 2020). The emission is highly sensitive to the gas density ( $\propto n_e^2$ ) and provides a valuable probe of the CGM distribution in galaxies.

The middle-left panel of Fig. 3 compares the soft X-ray (0.5 - 2 keV) surface brightness profiles predicted by the models. Note that

<sup>&</sup>lt;sup>3</sup>Except if significant rotation is present, see Stern et al. (2023).

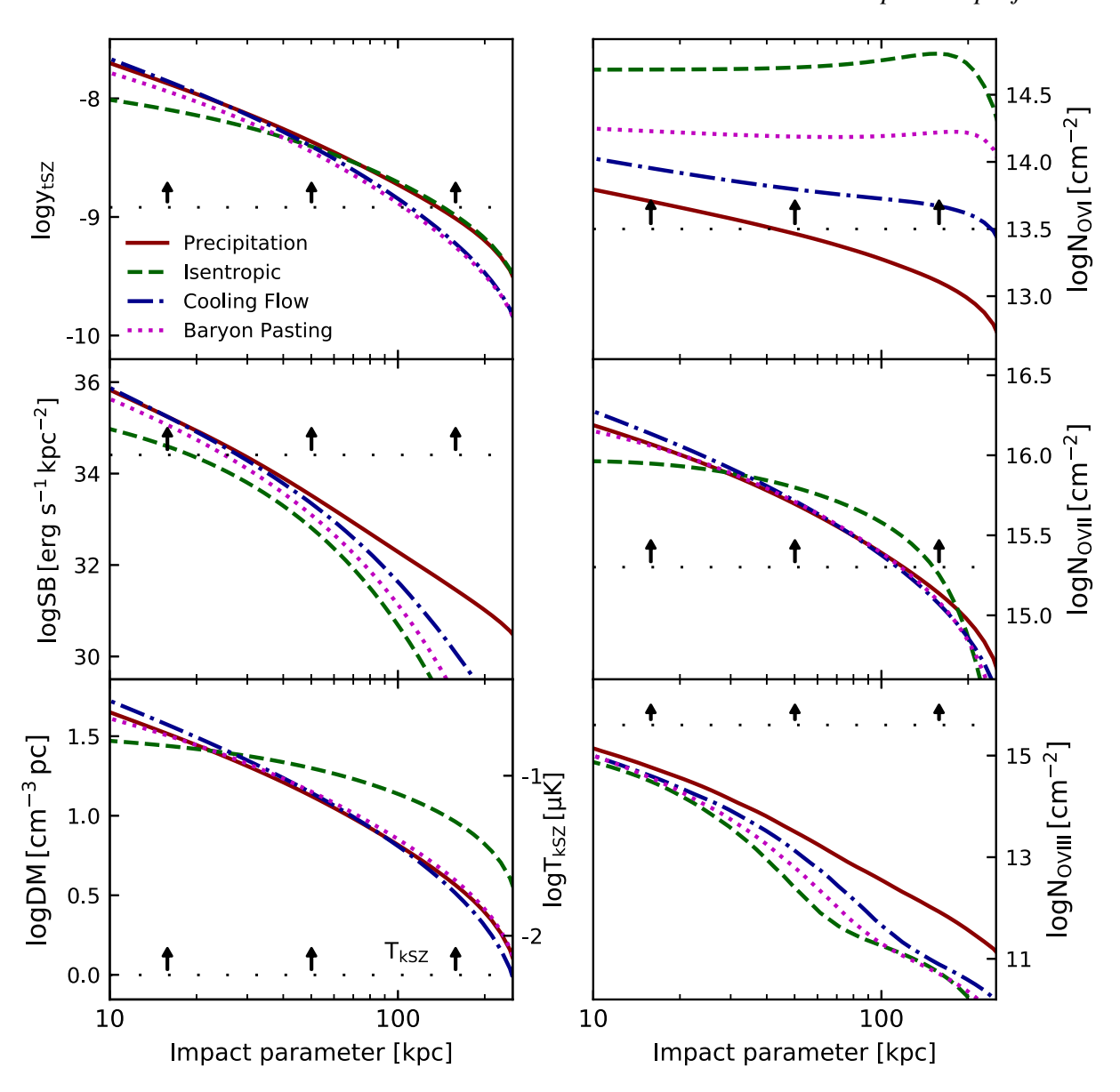


Figure 3. Comparison of the fiducial model's predictions for the projected tSZ effect (top left-hand panel), soft  $(0.5-2 \,\mathrm{keV})$  X-ray brightness (middle left-hand panel), dispersion measure and kSZ effect (bottom left-hand panel), and O VI, O VII, O VIII column densities (right-hand panels). Line styles and colours are as in Fig. 2. The combination of X-ray emission and dispersion measures and O VII and O VIII absorption lines shows complementary trends and, therefore, can also be used to constrain the thermodynamics of the CGM. The loosely dotted lines (with arrows) correspond to the tSZ sensitivity limit for CMB-S4 for a stack of  $\sim 300\,000$  galaxies at 150 GHz (top left-hand panel), eRASS4 sensitivity limit (radially averaged) for a stack of  $\approx 7\times10^4$  isolated MW mass galaxies with median redshift  $\approx 0.14$  from DESI Legacy survey (middle left-hand panel), kSZ sensitivity limit for CMB-S4 for a stack of  $\sim 100\,000$  galaxies at 150 GHz (bottom left-hand panel), COS-Haloes sensitivity limit for O VI (top-right panel), Athena/Arcus like mission sensitivity limits for O VII (middle-right panel), and O VIII (bottom-left panel) column densities for an individual absorber sightline.

the X-ray emission in a given energy band falls rapidly as the gas temperature moves away from the band. If the gas temperature is within the energy band considered, the X-ray emission is primarily dictated by the gas density. As a result, the model predictions for the X-ray surface brightness profiles trace the gas temperature at large radii and transition to tracing the gas density at smaller radii. The isentropic model gives the faintest X-ray halo due to low-gas densities at small radii and low-gas temperatures at large radii (see Fig. 2). The baryon pasting and cooling-flow models show similar X-ray emission profiles throughout the halo. The precipitation and cooling flow models predict similar X-ray emission out to 50 kpc,

beyond which the precipitation model takes over, thus predicting the brightest X-ray haloes within  $R_{\rm vir}$ . Therefore, measurements of X-ray surface brightness profiles near the virial radius (where the CGM densities are low) can be used to put stringent constraints on gas temperature and the thermal versus non-thermal components of a given CGM model.

However, measurement of the surface brightness beyond a few tens of kpc has been challenging because of the rapid signal decline with decreasing density. In the same panel, we show the average (over radial bins) sensitivity level for eRASS4 + DESI Legacy survey (Zhang et al. 2024) by stacking a sample of  $\approx 7 \times 10^4$ 

isolated MW mass (median  $M_*\approx 5.5\times 10^{10}{\rm M}_\odot$ ) galaxies with the median  $z\leq 0.14$ . For this sensitivity limit and our fiducial model parameters, the X-ray emission is detectable barely out to 20–30 kpc from the halo centre. The predicted X-ray emission profiles are sensitive to assumed virial mass and model-specific parameters. For example, Chadayammuri et al. (2022) measured the surface brightness at  $\gtrsim 100\,{\rm kpc}$  by stacking 2643 galaxies in the X-ray emission from the eFEDS survey (Brunner et al. 2022), and the stacked signal is dominated by brighter (and hence more massive than our fiducial model) galaxies. Furthermore, at temperatures of  $\sim 10^6\,{\rm K}$ , expected for the CGM of  $L_*$  galaxies, the emission in the soft X-ray is dominated by metal lines, and the degeneracy between gas metallicity and temperature limits the power of X-ray emission alone to simultaneously constrain the two (Anderson, Bregman & Dai 2013; Das et al. 2021).

#### 4.3 Fast radio bursts

The impact of the intervening ionized medium on the FRB signal causes a frequency-dependent delay in its arrival, represented by DM (e.g. McQuinn 2014; Ravi 2019; Chawla et al. 2022). The DM is thus sensitive to the ionized CGM and its dependence on feedback physics (e.g. Medlock et al. 2024). DM predictions for our models are plotted in the bottom-left panel of Fig. 3. The isentropic model also has a high DM due to the high-electron density at large radii, resulting from non-thermal pressure. The cooling flow, precipitation, and baryon pasting models are consistent with each other throughout the radial range. At large radii, near  $r \sim 100 - 150 \,\mathrm{kpc}$  (roughly half of the virial radius of the galaxy), the DM of the isentropic model is a factor of  $\sim 2$  higher than compared to the predictions for the other models. The isentropic model also predicts a flatter DM profile compared to the others, due to its flatter density profile. As noted above, the kSZ profile is identical to the DM signal (neglecting CGM rotation effects).

Presently available measurements of the DM are limited to more massive galaxies (Connor & Ravi 2022; Wu & McQuinn 2022) or only upper limits ( $\sim 100\,\mathrm{cm^{-3}}$  pc from Ravi et al. 2023 and  $\sim 200\,\mathrm{cm^{-3}}$  pc from Cook et al. 2023 for the MW CGM for an external observer at the solar circle), and are consistent with all four fiducial CGM models. Therefore, they cannot pinpoint CGM thermodynamics in  $L_*$  galaxies. We note that the measurement of DM from MW mass galaxies is not limited by the sensitivity limits of the corresponding missions (which are not shown in the figure) but by the limited spatial localization of FRB sightlines. The uncertainties in the contribution of the CGM to the total measured DM can only be improved with better FRB localizations and a large statistical sample of FRBs (Jankowski et al. 2023; Scott et al. 2023).

# 4.4 Absorption lines

Absorption line studies provide some of the most stringent constraints on the CGM mass in different phases, metallicity, ionization state, and the extent of the gas (Werk et al. 2013; Johnson, Chen & Mulchaey 2015; McQuinn & Werk 2018, Mathur 2022). High ions such as O VI, O VIII, O VIII, Ne VIII, and Fe XVII observed at UV and X-ray wavelengths are particularly useful for constraining warm/hot CGM (Bregman & Lloyd-Davies 2007; Tumlinson et al. 2011; Gupta et al. 2012; Burchett et al. 2019; Tchernyshyov et al. 2022; Qu et al. 2024).

In the right panels of Fig. 3, we show the predictions of the fiducial model for the column densities of O VI (top), O VII (middle), and O VIII (bottom). These column densities depend on the product of

gas density, metallicity, and ion fraction, where the ion fractions themselves depend on the gas properties and assumptions about the ionization mechanism. Throughout this work, we calculate the ion fractions using CLOUDY 17.00 (Ferland et al. 2017) assuming an optically thin gas in CIE, with the ion fractions functions of the gas temperature alone.<sup>4</sup>

The O VI ion fraction peaks at temperatures  $\sim 3 \times 10^5$  K in CIE. In the isentropic model, the gas temperature at large radii is close to this value, resulting in a high  $N_{\rm O\,VI}$ . As the CGM temperature at  $r>100\,\rm kpc$  in the precipitation model is a factor of  $\sim 2-3$  higher than in the isentropic model,  $N_{\rm O\,VI}$  decreases by more than an order of magnitude throughout the halo (see also Voit 2019 for the implications of temperature fluctuations on the density of the O VI column).  $N_{\rm O\,VI}$  predictions for the cooling flow and baryon pasting models lie in the range enclosed by the isentropic and precipitation models due to their intermediate gas temperatures.

The OVI column density detection limit for the COS-Haloes survey is  $\geq 3 \times 10^{13} \, \text{cm}^{-2}$  (Tumlinson et al. 2011), well below most of our predictions of the fiducial model, except at r > 40 kpc (see also Appendix A for a compilation of  $N_{\rm O\,\tiny VI}$  measurements). However, the models discussed here address the warm/hot phase of the CGM and do not include the cool- or intermediate-temperature gas. Previous work explored different scenarios to understand whether the OVI can originate in this lower-temperature gas. For example, Stern et al. (2018) suggested that it may reside in low-density cool photo-ionized gas outside the virial shock. Another suggestion was that the observed O VI may form in gas cooling from the ambient hot phase or in mixing layers between the hot and cool phases. However, Gnat & Sternberg (2004) showed that many interfaces are required to reproduce the O VI columns measured in the MW. Furthermore, Faerman & Werk (2023) showed that even a significant mass of intermediate temperature gas (similar to the cool gas mass) would only contribute  $\lesssim 10~{\rm per}$  cent to the O VI column measured in the COS-Haloes survey at large impact parameters.

The ionization fraction of O VII remains relatively constant and close to unity at temperatures  $T\sim 3\times 10^5-2\times 10^6$  K and falls rapidly outside of this range under the assumption of CIE. As a result,  $N_{\rm O\,VII}$  approximately follows the respective gas density profiles, with the isentropic model predicting the highest column densities beyond 30 kpc and out to the virial radius. On the other hand, the ionization fraction of O VIII peaks at  $T\sim 2\times 10^6$  K. Therefore, the precipitation model predicts the largest  $N_{\rm O\,VIII}$ . The isentropic, cooling flow, and baryon pasting models predict large values of  $N_{\rm O\,VIII}$  at T<30 kpc where the temperature is favourable for O VIII, followed by a rapid decline.

Currently, for O VII and O VIII, we are limited to column densities greater than  $10^{16}$  and  $2\times10^{15}$  cm $^{-2}$ , respectively, detected in absorption by the MW CGM (Bregman & Lloyd-Davies 2007; Gupta et al. 2012; Fang et al. 2015; Das et al. 2019a, Das et al. 2021). An Arcus (Smith et al. 2016) or Athena (Barret et al. 2016) like mission will be able to detect O VII column densities down to  $\geq 2\times10^{15}$  cm $^{-2}$  for individual galaxies (Wijers, Schaye & Oppenheimer 2020). The sensitivity limit is shown in the middleright panel of Fig. 3. Therefore, such missions will enable us to detect O VII in MW-like galaxies out to the virial radii and constrain the gas density distributions approximately independently of the temperature profile. LEM (Kraft et al. 2022) will allow us to probe these lines

<sup>4</sup>We note that at low-gas densities in the CGM, photoionization by the metagalactic radiation field can be significant even for the high ions discussed here and at low redshift (see discussion in FSM20 and Faerman et al. 2022).

in X-ray emission beyond the virial radii for individual MW mass galaxies. Although the O VIII column density detection limits for these missions ( $\geq 4 \times 10^{15} \, \mathrm{cm}^{-2}$ ) are higher than the fiducial model predictions, the sensitivity limit can be reduced by an order of magnitude or more by stacking a large number of galaxies.

In Appendix A, we provide a qualitative comparison of our model predictions with currently available data sets for  $L_*$  and massive galaxies, including model parameter uncertainties. Our publicly available Python toolkit<sup>5</sup> allows us to compute these observables, provided the CGM density, temperature, and metallicity profiles.

#### 5 SUMMARY

Idealized CGM models provide an intuitive method to constrain physical processes in the CGM. In this paper, we compare the thermodynamic profiles of the CGM for the precipitation, isentropic, cooling flow, and baryon pasting models. Each CGM model considered here solves Euler's fluid equations under model-specific assumptions (see Fig. 1 for illustration). We computed the entropy, electron density, gas pressure, and temperature profiles (Fig. 2) for the four fiducial models for a MW mass galaxy ( $M_{\rm vir}=10^{12}\,{\rm M}_{\odot},z\sim0$ ) in an NFW + galaxy potential with concentration  $c_{vir} = 10$ ,  $M_* =$  $6 \times 10^{10} \,\mathrm{M}_{\odot}$ . We assume a gas in the CIE with a constant metallicity of 0.3  $Z_{\odot}$ . The models show the most significant differences in the entropy and temperature profiles at small ( $r \lesssim 30 \,\mathrm{kpc}$ ) and large  $(r \ge 100 \,\mathrm{kpc})$  galactocentric distances. Specifically, the precipitation model predicts comparatively high-entropy, high-temperature ( $T \sim$  $10^6$  K), and low-CGM density beyond  $\gtrsim 50$  kpc. The predictions of the cooling flow model are close to those of the precipitation model for the radii within the cooling radius ( $r \leq 100 \,\mathrm{kpc}$ ) where it is potentially valid. The isentropic model predicts relatively flatter profiles (except temperature), while the baryon pasting model shows a distinctively cored temperature profile at  $r < 30 \,\mathrm{kpc}$ .

We then addressed the observable quantities predicted by the fiducial models and compared the SZ effect, soft X-ray emission, DM probed by FRBs, and oxygen column densities for O VI, O VII, and O VIII, measured in UV and X-ray absorption (Fig. 3). These observables trace different combinations of the thermodynamic quantities, and their combinations can be used to constrain the underlying CGM physical properties. We used the same set of input parameters for each model, thus making sure that any differences in the predicted thermodynamic or observable quantities are due to the inherent differences in the model assumptions.

The tSZ profiles trace the projected pressure profiles, differing by a factor of two near the galactic centre and its outskirt. Stacking  $\sim 300\,000$  galaxies with CMB-S4 could detect and resolve the tSZ signature predicted by the four fiducial models up to 100 kpc. In the case of the kSZ effect, the sensitivity level required to probe the signal out to the virial radius can be achieved by stacking  $\sim$ 100 000 galaxies in CMB-S4 provided accurate peculiar velocity measurements. O VII column density traces the gas density profile in the temperature range  $T \sim 3 \times 10^5 - 2 \times 10^6$  K, which, in fact, captures the variety of temperature profiles predicted by these distinct models. The O VII column density signal predicted by the models can be detected out to 100 kpc for individual galaxies for Athena/Arcuslike missions. The soft X-ray emission shows distinct predictions for the precipitation and the isentropic models, where the former produces at least an order of magnitude brighter X-ray haloes than the latter. The current model predictions for the X-ray surface brightness are lower than the eROSITA detection limits, highlighting the need

for deeper X-ray surveys. The models also predict unique FRB DM profiles, where the combination of DM and soft X-ray emission displays the ability to differentiate between the precipitation and the isentropic models. Compared to the other models, the cooling flow model predicts steeper observable profiles in most cases (except for O VIII). Our results show that the amplitude of the kSZ effect is dominant (for typical peculiar velocities of  $\approx 300~{\rm km\,s^{-1}}$ ) compared to that of the tSZ effect in MW mass galaxies for all four CGM models (although it is more challenging to separate the kSZ signal from CMB fluctuations since there is no associated change in the spectrum). O VI column density predictions also show stark differences between the CGM models, although potential contributions from additional phases may complicate the interpretation of this observable (see Section 4.4).

We showed that combining entropy and temperature profiles allows one to assess the relative importance of the physical processes in the different CGM models. Still, we need a combination of observables to do so. For example, tSZ alone is not a good diagnostic of CGM physics due to the similar predictions by very different models. However, when combined with the FRB dispersion measure or the kSZ signal, they can constrain both the temperature and entropy of the CGM ( $K(r) \propto \text{tSZ/DM}^{5/3}$  and  $T(r) \propto \text{tSZ/DM}$ ). Similarly, the combination of the O VII and O VIII column densities is particularly useful for simultaneously constraining the density and temperature of the CGM due to the sensitivity of the ion fractions to the gas temperature.

The Python package we used for computing the observables from the CGM models is made publicly available. It can be used easily to add another CGM model to this comparison with the code. It presents a unique platform for forward modelling the CGM observables from its thermodynamic properties.

There are several ongoing and next-generation missions planned with the CGM as one of the key science goals, with observations across the electromagnetic spectrum. In this work, we bring different idealized CGM models on to a single platform, and the accompanying pipeline will be useful for modelling and interpreting a plethora of multiwavelength CGM observations, allowing a direct comparison of their data sets with a variety of easily tunable CGM physics realizations. Such an analysis is also essential to harness the capabilities of next-generation multiwavelength missions as a community by differentiating CGM models with strikingly different assumptions on CGM physics.

# ACKNOWLEDGEMENTS

We thank the referee for valuable suggestions and comments. We thank Mark G. Voit, Benjamin D. Oppenheimer, Nicholas Battaglia, Yi Zhang, Srinivasan Raghunathan, and Zhijie Qu for the helpful discussions. We gratefully acknowledge the hospitality and discussions at 'Fundamentals of Gaseous Haloes' conference at the Kavli Institute for Theoretical Physics (KITP), which was supported in part by the National Science Foundation (NSF) under Grant No. NSFPHY-1748958. PS acknowledges support from the YCAA Prize Postdoctoral Fellowship and the Yale Center for Research Computing facilities and staff. YF was supported by NASA award 19-ATP19-0023 and NSF award AST-2007012. JS was supported by the Israel Science Foundation (Grant No. 2584/21). DN was supported by the NSF award AST 2206055.

# DATA AVAILABILITY

The data sets underlying this article are publicly available or available via the authors of their respective publications.

<sup>&</sup>lt;sup>5</sup>https://github.com/ethlau/cgm\_toolkit

#### REFERENCES

Abazajian K. N. et al., 2016, preprint (arXiv:1610.02743)

Ade P. et al., 2019, J. Cosmol. Astropart. Phys., 2019, 056

Amodeo S. et al., 2021, Phys. Rev. D, 103, 063514

Anderson M. E., Bregman J. N., 2011, ApJ, 737, 22

Anderson M. E., Bregman J. N., Dai X., 2013, ApJ, 762, 106

Anderson M. E., Churazov E., Bregman J. N., 2016, MNRAS, 455, 227

Aung H., Nagai D., Lau E. T., 2021, MNRAS, 508, 2071

Barret D. et al., 2016, in den Herder J.-W. A., Takahashi T., Bautz M., eds, Proc. SPIE Conf. Ser. Vol. 9905, Space Telescopes and Instrumentation 2016: Ultraviolet to Gamma Ray. SPIE, Bellingham, p. 99052F

Battaglia N. et al., 2019, BAAS, 51, 297

Battaglia N., Ferraro S., Schaan E., Spergel D. N., 2017, J. Cosmol. Astropart. Phys., 2017, 040

Benson B. A. et al., 2014, in Holland W. S., Zmuidzinas J., eds, Proc. SPIE Conf. Ser. Vol. 9153, Millimeter, Submillimeter, and Far-Infrared Detectors and Instrumentation for Astronomy VII. SPIE, Bellingham, p. 91531P

Bogdán Á., Bourdin H., Forman W. R., Kraft R. P., Vogelsberger M., Hernquist L., Springel V., 2017, ApJ, 850, 98

Bregman J. N., Hodges-Kluck E., Qu Z., Pratt C., Li J.-T., Yun Y., 2022, ApJ, 928, 14

Bregman J. N., Lloyd-Davies E. J., 2007, ApJ, 669, 990

Brunner H. et al., 2022, A&A, 661, A1

Burchett J. N. et al., 2019, ApJ, 877, L20

Butler Contreras A., Lau E. T., Oppenheimer B. D., Bogdán Á., Tillman M., Nagai D., Kovács O. E., Burkhart B., 2023, MNRAS, 519, 2251

Chadayammuri U., Bogdán Á., Oppenheimer B. D., Kraft R. P., Forman W. R., Jones C., 2022, ApJ, 936, L15

Chawla P. et al., 2022, ApJ, 927, 35

Chen H.-W. et al., 2020, MNRAS, 497, 498

CHIME/FRB Collaboration, 2018, ApJ, 863, 48

Choudhury P. P., Sharma P., Quataert E., 2019, MNRAS, 488, 3195

Comparat J. et al., 2022, A&A, 666, A156

Connor L., Ravi V., 2022, Nat. Astron., 6, 1035

Cook A. M. et al., 2023, ApJ, 946, 58

Das S., Mathur S., Gupta A., 2020, ApJ, 897, 63

Das S., Mathur S., Gupta A., Krongold Y., 2021, ApJ, 918, 83

Das S., Mathur S., Nicastro F., Krongold Y., 2019a, ApJ, 882, L23

Das, S., Mathur, S., Gupta, A., et al.. 2019b, ApJ, 885, 108

Faerman Y., Pandya V., Somerville R. S., Sternberg A., 2022, ApJ, 928, 37

Faerman Y., Sternberg A., McKee C. F., 2017, ApJ, 835, 52

Faerman Y., Sternberg A., McKee C. F., 2020, ApJ, 893, 82 (FSM20)

Faerman Y., Werk J. K., 2023, ApJ, 956, 92

Fang T., Buote D., Bullock J., Ma R., 2015, ApJS, 217, 21

Ferland G. J. et al., 2017, Rev. Mex. Astron. Astrofis., 53, 385

Flender S., Nagai D., McDonald M., 2017, ApJ, 837, 124

Gnat O., Sternberg A., 2004, ApJ, 608, 229

Gupta A., Mathur S., Krongold Y., Nicastro F., Galeazzi M., 2012, ApJ, 756, L8

Haardt F., Madau P., 2012, ApJ, 746, 125

Hafen Z. et al., 2019, MNRAS, 488, 1248

Henderson S. W. et al., 2016, J. Low Temp. Phys., 184, 772

Hummels C. B. et al., 2019, ApJ, 882, 156

Jankowski F. et al., 2023, MNRAS, 524, 4275

Johnson S. D., Chen H.-W., Mulchaey J. S., 2015, MNRAS, 449, 3263

Kraft R. et al., 2022, preprint (arXiv:2211.09827)

Kravtsov A. V., Vikhlinin A. A., Meshcheryakov A. V., 2018, Astron. Lett., 44, 8

Lee E. et al., 2022, MNRAS, 517, 5303

Lee M. E. et al., 2024, ApJ, 968, 11

Lehner N., Howk J. C., Wakker B. P., 2015, ApJ, 804, 79

Li J.-T., Bregman J. N., Wang Q. D., Crain R. A., Anderson M. E., 2018, ApJ, 855, L24

Lim S. H., Barnes D., Vogelsberger M., Mo H. J., Nelson D., Pillepich A., Dolag K., Marinacci F., 2021, MNRAS, 504, 5131 Mathur S., 2022, In Bambi C., Santangelo A., eds, Hand-book of X-ray and Gamma-ray Astrophysics. Springer, Singapore, p. 112

McQuinn M., 2014, ApJ, 780, L33

McQuinn M., Werk J. K., 2018, ApJ, 852, 33

Medlock I., Nagai D., Singh P., Oppenheimer B., Anglés Alcázar D., Villaescusa-Navarro F., 2024, ApJ, 967, 32

Moser E. et al., 2022, ApJ, 933, 133

Mowla L., van der Wel A., van Dokkum P., Miller T. B., 2019, ApJ, 872, L13

Nelson K., Lau E. T., Nagai D., 2014, ApJ, 792, 25

Newburgh L. B. et al., 2016, in Hall H. J., Gilmozzi R., Marshall H. K., eds, Proc. SPIE Conf. Ser. Vol. 9906, Ground-based and Airborne Telescopes VI. SPIE, Bellingham, p. 99065X

Ni Y. et al., 2023, ApJ, 959, 136

Oppenheimer B. D., 2018, MNRAS, 480, 2963

Osato K., Nagai D., 2022, MNRAS, 519, 2069

Ostriker J. P., Bode P., Babul A., 2005, ApJ, 634, 964

Pandya V. et al., 2023, ApJ, 956, 118

Peeples M. S. et al., 2019, ApJ, 873, 129

Prochaska J. X., Zheng Y., 2019, MNRAS, 485, 648

Qu Z. et al., 2024, ApJ, 968, 8

Qu Z., Bregman J. N., 2018, ApJ, 856, 5

Ramesh R., Nelson D., 2024, MNRAS, 528, 3320

Ravi V. et al., 2023, preprint (arXiv:2301.01000)

Ravi V., 2019, ApJ, 872, 88

Ried Guachalla B., Schaan E., Hadzhiyska B., Ferraro S., 2023, Phys. Rev. D, 109, 103533

Schaan E. et al., 2021, Phys. Rev. D, 103, 063513

Scott D. R. et al., 2023, Astron. Comput., 44, 100724

Sharma P., McCourt M., Parrish I. J., Quataert E., 2012, MNRAS, 427, 1219

Shaw L. D., Nagai D., Bhattacharya S., Lau E. T., 2010, ApJ, 725, 1452

Shi X., 2016, MNRAS, 461, 1804

Shirasaki M., Lau E. T., Nagai D., 2020, MNRAS, 491, 235

Singh P., Voit G. M., Nath B. B., 2021, MNRAS, 501, 2467

Smith R. K. et al., 2016, in den Herder J.-W. A., Takahashi T., Bautz M., eds, Proc. SPIE Conf. Ser. Vol. 9905, Space Telescopes and Instrumentation 2016: Ultraviolet to Gamma Ray. SPIE, Bellingham, p. 99054M

Stern J., Faucher-Giguère C.-A., Hennawi J. F., Hafen Z., Johnson S. D., Fielding D., 2018, ApJ, 865, 91

Stern J., Fielding D., Faucher-Giguère C.-A., Quataert E., 2019, MNRAS, 488, 2549

Stern J., Fielding D., Faucher-Giguère C.-A., Quataert E., 2020, MNRAS, 492, 6042

Stern J., Fielding D., Hafen Z., Su K.-Y., Naor N., Faucher-Giguère C.-A., Quataert E., Bullock J., 2023, MNRAS, 530, 1711

Sunyaev R. A., Zeldovich Y. B., 1972, Comment. Astrophys. Space Phys., 4, 173

Tanimura H., Aghanim N., Bonjean V., Zaroubi S., 2022, A&A, 662, A48

Tchernyshyov K. et al., 2022, ApJ, 927, 147

Tumlinson J. et al., 2011, Science, 334, 948

Tumlinson J., Peeples M. S., Werk J. K., 2017, ARA&A, 55, 389

van de Voort F., Springel V., Mandelker N., van den Bosch F. C., Pakmor R., 2019, MNRAS, 482, L85

Villaescusa-Navarro F. et al., 2021, ApJ, 915, 71

Voit G. M., 2005, Rev. Mod. Phys., 77, 207

Voit G. M., 2019, ApJ, 880, 139

Voit G. M., Ma C. P., Greene J., Goulding A., Pandya V., Donahue M., Sun M., 2018, ApJ, 853, 78

Voit G. M., Meece G., Li Y., O'Shea B. W., Bryan G. L., Donahue M., 2017, ApJ, 845, 80

Werk J. K., Prochaska J. X., Thom C., Tumlinson J., Tripp T. M., O'Meara J. M., Peeples M. S., 2013, ApJS, 204, 17

Wijers N. A., Schaye J., Oppenheimer B. D., 2020, MNRAS, 498, 574

Wu X., McQuinn M., 2022, ApJ, 945, 87

Yang T., Cai Y.-C., Cui W., Davé R., Peacock J. A., Sorini D., 2022, MNRAS, 516, 4084

Zhang Y. et al., 2024, preprint (arXiv:2401.17308)

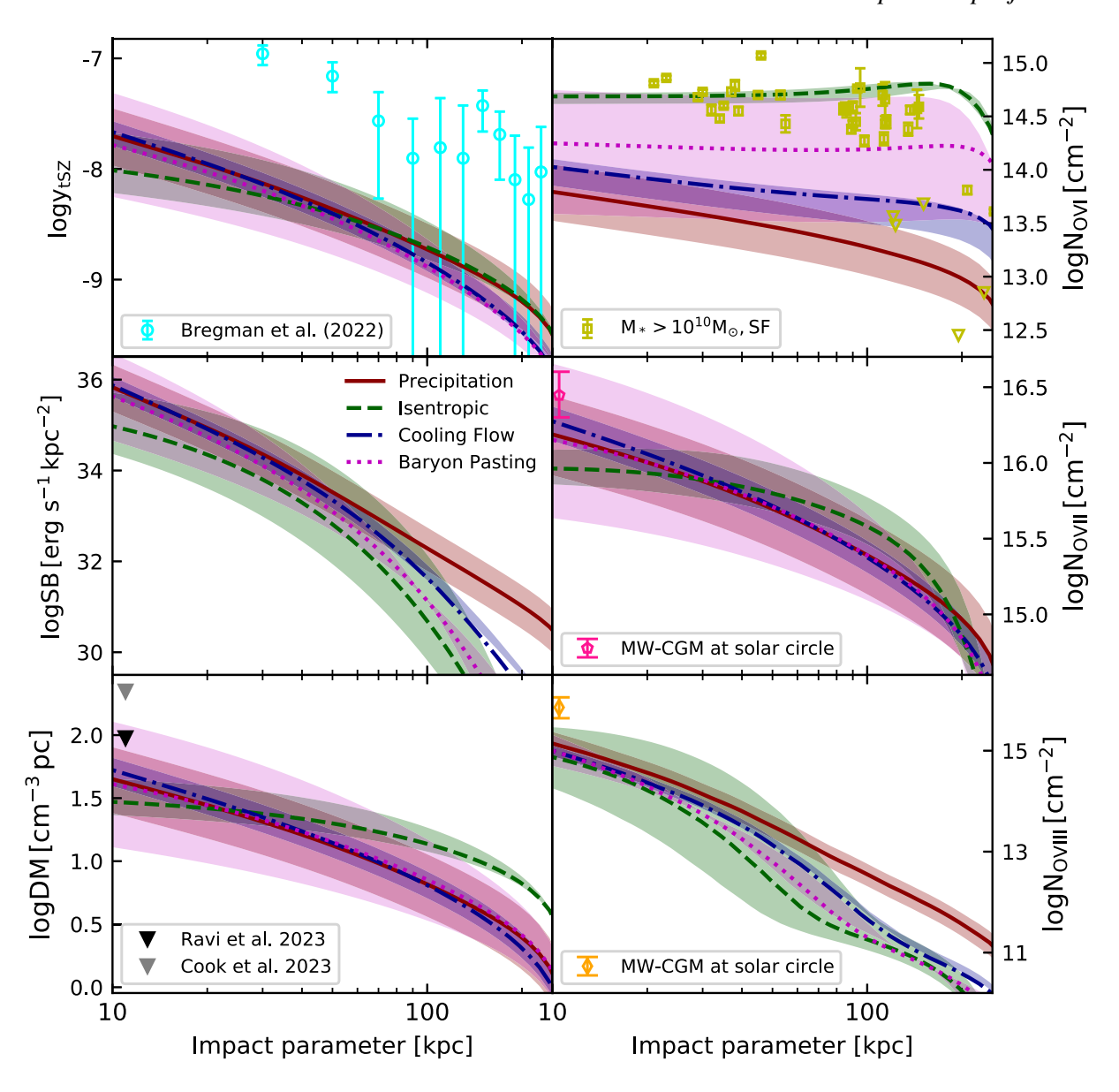


Figure A1. Same as Fig. 3 with the shaded regions around each of the predictions of the fiducial model representing the uncertainties in the model-specific parameters as discussed in Section A. The cyan circles in the top-left panel show the stacked tSZ signal for  $L_*$  galaxies (Bregman et al. 2022). The yellow squares (triangles) in the top-right panel show O VI column density measurements (upper limits) from COS-Haloes (Tumlinson et al. 2011) and eCGM surveys (Johnson et al. 2015). The pink hexagon (middle-right panel) and orange diamond (bottom-right panel) are the O VII (Bregman & Lloyd-Davies 2007; Fang et al. 2015; Das et al.) and O VIII (Gupta et al. 2012; Das et al. 2019a) column density measurements, respectively, for MW at the solar circle, multiplied by a factor of two to compare with model predictions of projected column densities as an external observer. In the lower left-hand panel, black and grey triangles represent the upper limits of the MW-CGM dispersion measure from a localized FRB in the Deep Synoptic Array (Ravi et al. 2023) and the CHIME-FRB catalogue (Cook et al. 2023), respectively, for an external observer at the solar circle.

# APPENDIX A: OBSERVABLE DEPENDENCE ON MODEL-SPECIFIC PARAMETERS

In Section 4, we compared the predictions of the CGM models using the fiducial values of model parameters. Many of these model parameters significantly affect the normalization and shape of the observed profiles. In Fig. A1, we include a range in the model-specific parameters to highlight their impact on observable quantities. We list the parameters varied and their ranges in Table A1.

In addition, we compile many of the currently available CGM observations and show them in Fig. A1. Note that some of these measurements are limited to more massive galaxies than our fiducial choice, span a range in redshifts, and may suffer from Malmquist bias due to the stacking procedure, and therefore are meant for a qualitative rather than a quantitative comparison with the model predictions.

The tSZ data (cyan circles in the top-left panel) are taken from Bregman et al. (2022, see fig. 8). They represent the dimensionless y-parameter measured from the *Planck* and *WMAP* data sets by stacking 11  $L_*$  galaxies in the local Universe with distance < 10 Mpc (i.e. z < 0.003). The median stellar mass of the sample is  $\sim 6.8 \times 10^{10}$  M $_{\odot}$ 

<sup>&</sup>lt;sup>6</sup>For the isentropic model, we only show the variation in  $\alpha$  in Fig. A1 for simplicity.

# 3234 *P. Singh et al.*

**Table A1.** Dependence of observable quantities ( $\alpha_{PL}$ ) on model-specific input parameters near the inner ( $\approx$ 50 kpc) and the outer ( $\approx$ 150 kpc) CGM.

|                                     |         | Precipitation                    | Isentropic                            |            | Cooling flow                             | Baryon pasting                      |
|-------------------------------------|---------|----------------------------------|---------------------------------------|------------|--|-------------------------------------|
|                                     |         | $t_{\rm cool}/t_{\rm ff}$ [5,20] | $\sigma_{turb}$ [20,100] $(kms^{-1})$ | α<br>[1,3] | $\dot{M}$ [0.5,1.5] $(M_{\odot} y^{-1})$ | $10^{6} \epsilon_{\rm f}$ [0.5,1.5] |
| tSZ                                 | 50 kpc  | -0.8                             | -0.4                                  | -0.9       | 0.5                                      | -1.2                                |
|                                     | 150 kpc | -                                | -0.2                                  | -0.3       | -  | -0.7                                |
| DM                                  | 50 kpc  | -0.8                             | -0.2                                  | -0.5       | 0.5                                      | -1.4                                |
|                                     | 150 kpc | _                                | -0.1                                  | -0.2       | _  | -1                                  |
| XSB [0.5–2.0] keV                   | 50 kpc  | -1.6                             | -1.3                                  | -3.7       | 1  | -1.6                                |
|                                     | 150 kpc | _                                | -1.5                                  | -4.1       | _  | 2.4                                 |
| $N_{ m O{\scriptscriptstyle VI}}$   | 50 kpc  | -0.9                             | 0.1                                   | 0.3        | 0.5                                      | -1.7                                |
|                                     | 150 kpc | _                                | 0.1                                   | -0.1       | _  | -1.6                                |
| $N_{ m O{\scriptscriptstyle VII}}$  | 50 kpc  | -0.8                             | -0.3                                  | -0.7       | 0.5                                      | -1.3                                |
|                                     | 150 kpc | _                                | -0.4                                  | -0.9       | _  | -0.7                                |
| $N_{ m O{\scriptscriptstyle VIII}}$ | 50 kpc  | -0.8                             | -1.4                                  | -4.3       | 0.5                                      | 1                                   |
|                                     | 150 kpc | -                                | -0.6                                  | -1.1       | _  | $\approx 0$                         |

corresponding to an approximate virial mass  $\sim 2 \times 10^{12}~M_{\odot}$  (two times the fiducial mass assumed for the models in our work). All four fiducial CGM models lie an order of magnitude below the tSZ signal, likely driven by the more massive and hotter haloes in the observational data set ( $y \propto M_{\rm vir}^{5/3}$ ).

The O VI absorption line column densities (yellow squares and triangles in the top-right panel) are taken from COS-Haloes (Tumlinson et al. 2011) and eCGM surveys (Johnson et al. 2015), using only absorption features associated with late-type, isolated galaxies with stellar masses above 1010 Mo. These galaxies span a redshift range 0.1-0.4 with a median stellar mass of  $2.8\times10^{10}\,\mathrm{M}_{\odot}$  corresponding to a median halo mass of  $\sim 10^{12}~{\rm M}_\odot$  (Kravtsov, Vikhlinin & Meshcheryakov 2018; Mowla et al. 2019). The fiducial isentropic model is calibrated to reproduce  $N_{OVI}$ , whereas other models are not, lying one to two orders of magnitude below the column density measurements. Qu et al. (2024) report O VI absorption in the CGM of galaxies at 0.4 < z < 0.7. For the massive star forming galaxies in their sample, they find that the combined column density profile can be fit with  $\log(N_{\rm O\,VI}(b=R_{200})) = 14.20 \pm 0.09$  and a slope of  $0.74 \pm 0.21$  (see their fig. 9 and table 2). The baryon pasting and isentropic models produce similar column densities and flatter profiles, while the precipitation model has a more similar slope and lower column densities. We note that the galaxy sample described by Qu et al. (2024) is at higher redshifts than our models, and the slope they infer might be affected by column densities at impact parameters  $\approx r_{200}$ .

The column densities of O VII (pink hexagon in the middle-right panel) and O VIII (orange diamond in the bottom-right panel) are the measurements of MW-CGM in the solar circle (Bregman & Lloyd-Davies 2007; Gupta et al. 2012; Fang et al. 2015; Das et al. 2019a). We multiplied the observed column densities by a factor of two to mimic the projected column densities as an external observer. As shown in Fig. A1, the precipitation, cooling flow, and baryon pasting models produce higher OVII columns due to their higher central densities than the isentropic model. All four fiducial models underestimate O VIII. We note that the fiducial isentropic model described in FSM20 has a solar metallicity in the inner CGM, and matches the O VII and O VIII columns measured in the MW (see their table 2). This demonstrates that the ion column densities are sensitive to modelling assumptions such as ionization equilibrium, metallicity distribution, and an external radiation field (e.g. see fig. 6 in Faerman et al. 2022). A full exploration of how individual model predictions

vary with such modelling assumptions is beyond the scope of this work.

Ravi et al. (2023) derived an upper limit on the DM contribution by the MW-CGM using a recently discovered non-repeating FRB (20220319D) from the Deep Synoptic Array. The limit is shown by the black triangle in the lower-left panel of Fig. A1 for an external observer with the impact parameter passing through the solar circle. The upper limit can decrease by 40 per cent depending on the value they use for ISM contamination of the DM. The grey triangle in the same panel corresponds to the upper limit derived by Cook et al. (2023) using the CHIME-FRB catalogue. Their upper limit can decrease by 50 per cent depending on their ISM contamination model. All four CGM models considered here are consistent with the two measurements.

We also attempt to capture the dependence of tSZ, DM,<sup>7</sup> soft X-ray emission, and oxygen absorption column densities on the model parameters near the inner ( $\sim 50\,\mathrm{kpc}$ ) and outer ( $\sim 150\,\mathrm{kpc}$ ) CGM. To quantify the dependence of a given observable O on a particular model parameter P, we calculate the power-law slope  $\alpha_{\mathrm{PL}}$  defined as  $O \propto P^{\alpha_{\mathrm{PL}}}$  (with fixed boundary conditions). We tabulate the values  $\alpha_{\mathrm{PL}}$  in Table A1.

In the case of the precipitation model, the X-ray emission is more sensitive to the value of  $t_{\rm cool}/t_{\rm ff}$  with  $\alpha_{\rm PL} \sim -1.6$ , while other observables show very similar values of  $\alpha_{PL}(\sim -0.8)$ , making the X-ray emission the most optimal tool for constraining  $t_{\rm cool}/t_{\rm ff}$ . These trends are driven by the density dependence of the observables, since the temperature does not vary significantly due to the fixed boundary condition. The sensitivity to  $t_{\rm cool}/t_{\rm ff}$  does not depend on the radial distance of any observables considered here. The cooling flow model mimics the trends seen in the precipitation model with  $\alpha_{PL} \sim 1$  for X-ray emission and  $\sim 0.5$  for other observables. These results further highlight the need for deeper X-ray surveys. In the case of baryon pasting,  $\epsilon_{\rm f}$  has the strongest impact on X-ray emission ( $\alpha_{\rm PL} \sim -1.6$ at 50 kpc and  $\sim 2.4$  at 150 kpc). For most other observables, the levels of sensitivity range from  $\alpha_{\rm PL} \sim -1$  to -2 (except O VIII). The isentropic model shows more interesting trends as a function of the input parameters and the radial range. For example,  $N_{OVI}$  shows an opposite trend to other observables as a function of  $\sigma_{turb}$  and  $\alpha$ . X-

<sup>&</sup>lt;sup>7</sup>We do not show the parameter dependencies for kSZ since it is identical to DM.

ray emission and  $N_{\rm O\,{\tiny VIII}}$  are most sensitive to the model parameters. These trends are due to a peak in their respective ion fractions in a narrow temperature range (see Faerman et al. 2022 for more details).

The purpose of the analysis and the results shown in Fig. A1 and Table A1 is to identify the model parameters to which the observable

quantities are most sensitive, helping in planning the most effective strategy to select observations to constrain CGM physics.

This paper has been typeset from a TEX/IATEX file prepared by the author.